

ON THE STABILITY OF THE DUAL PROBLEM FOR HIGH REYNOLDS NUMBER FLOW PAST A CIRCULAR CYLINDER IN TWO DIMENSIONS*

MURTAZO NAZAROV[†] AND JOHAN HOFFMAN[‡]

Abstract. In this paper we present a computational study of the stability of time dependent dual problems for compressible flow at high Reynolds numbers in 2D. The dual problem measures the sensitivity of an output functional with respect to numerical errors, and is a key part of goal oriented a posteriori error estimation. Our investigation shows that the dual problem associated with the computation of the drag force for the compressible Euler/Navier-Stokes equations, which are approximated numerically using different temporal discretization and stabilization techniques, is unstable and exhibit blowup for several Mach regimes considered in this paper.

Key words. stability, Euler equations, Navier-Stokes equations, circular cylinder, dual equations, goal-oriented error estimation

AMS subject classifications. 65M60

1. Introduction. Fluid flow at various Reynolds numbers (Re) and Mach numbers (M) is described by the Navier-Stokes equations (NSE). The dual (adjoint) NSE, linearized at primal solutions to NSE, can be used to characterize the effect of local errors on output functionals of the solution of interest for particular approximations, e.g. drag and lift of an aircraft, and the stability of the dual equations is a necessary part of goal oriented a posteriori error estimation. Over the last 15 years adaptive finite element methods based on a posteriori error estimation have been developed for a number of applications, see e.g. [8, 5, 10, 31, 30], including time dependent simulations of fluid flow described by NSE, see e.g. [2, 29, 18, 19]. Many problems have been resolved, and impressive results have been presented in terms of accuracy and efficiency. Even so, for time dependent flow problems several challenges remain, including reliable approximation of the dual NSE with respect to computational and linearization errors.

In particular, for high Reynolds numbers in 2D, blowup in the dual problem has been observed by Barth [3] in the sense that solutions to the dual NSE increase rapidly as the Reynolds number is increased. For stationary problems in 2D, no such blowup of dual solutions has been reported to the knowledge of the authors, see e.g. [13, 14, 25, 6]. One question is then if: (i) such blowup is a result of an inadequate numerical method used to discretize the continuous dual NSE, or (ii) if it is a consequence of an unstable continuous dual problem, possibly due to an unstable underlying primal solution. In the case (i), blowup in the dual NSE and thereby also the a posteriori error estimates is misleading, whereas in the case (ii) it may be an indication of an incomputable output functional for the problem at hand. On the other hand, (ii) may also be connected to a linearization error from approximation of the primal problem in the computation of the dual problem, and thus again be misleading with respect to error estimation.

*This material is based upon work supported by the European Research Council, the Swedish Research Council (VR) and the Swedish Foundation for Strategic Research (SSF).

[†]Corresponding author. Department of Mathematics, Texas A&M University 3368 TAMU, College Station, TX 77843, USA (murtazo@math.tamu.edu)

[‡]Computational Technology Laboratory, School of Computer Science and Communication, KTH, 100 44 Stockholm, Sweden (jhoffman@csc.kth.se)

The Euler equations (EE) correspond to NSE without the viscous terms, and without a viscous boundary layer, as an approximation of high Reynolds number Re flow, say $Re \geq 10^4$. In this paper we study the stability of the dual NSE and the dual EE associated with the computation of the drag force as a target functional for flow past a circular cylinder in 2D for various Mach numbers. We observe that for some Mach numbers, beyond a certain mesh resolution, numerical approximations to the dual problem become increasingly unstable as the mesh is refined, to eventually lead to blowup in time where the dual solution no longer can be advanced in time. The blowup is localized to spatial regions that correspond to certain flow features in the primal solution, at which the dual problem is linearized. For the inviscid EE the instabilities appear to be associated with separation, near attached shocks. Similarly, for NSE with no slip boundary conditions, separation from the boundary layer appears to be the source of instability. When blowup is detected in the dual solution, the underlying primal flow also shows strong vorticity production near separation.

To the knowledge of the authors, no such blowup of the dual problem have been reported in the literature for computed solutions in 3D. In fact, we have carried out a number of simulations in 3D for time dependent problems, including turbulent flow, where no blowup has been observed, see e.g. [20, 17, 18, 19]. For compressible flow, our computations have been limited to moderately fine meshes [28], but for incompressible flow, simulations with millions of mesh points have shown no blowup in the dual solution [32, 23]. On the other hand, trying to solve the dual problem linearized at a manufactured unstable solution leads to blowup also for incompressible flow in 3D, see e.g. [21] (Section 19.5).

Fluid flow past a circular cylinder is one of the most well studied problems in fluid mechanics, and serves as a model problem for a number of important applications. High Mach number inviscid compressible flow develops discontinuities, such as shocks where kinetic energy is dissipated. As the Mach number decreases the flow becomes less compressible, and eventually the discontinuities disappear. Experimentally, high Reynolds number flow at low Mach numbers past a cylinder is characterized by the development of a turbulent wake dissipating kinetic energy through vortex stretching, where the stretched vortices are made thinner to eventually dissipate into heat when the length scale approaches the Kolmogorov microscale. Turbulence with vortex stretching is a 3D effect, which cannot be modeled by the 2D equations. It is one important difference between 2D and 3D flows. Vortex stretching is the basic mechanism of turbulent flow to transfer energy from large to small scales, to eventually be dissipated at the small viscous scales. In 2D, turbulent dissipation in this form is not possible. For high Re , the only dissipative mechanism in 2D is energy loss in shocks. For low Mach numbers, dissipation in shocks is low, whereas for high Mach numbers it can be significant.

In our computational experiments we observe that the formation of very sharp gradients and high vorticity production, in boundary layers or near (numerically smeared) discontinuities, is correlated with blowup in the dual problem. In physical experiments, this class of 2D flows are rarely found, instead 3D features develop, likely as a reaction to instabilities [33]. The contribution of this paper is a computational study that can lead to new insights into the stability of the dual NSE, limitations in the a posteriori error estimation framework that relies on the computational approximation of dual problems, the computability of compressible flow in 2D, and possibly also of the limitations of 2D flow models. In particular, some key differences to 3D flow are highlighted.

In future work we will follow up this study for more problems, to get a better understanding of the stability of the dual equations, including their dependency on various flow parameters. We will also perform similar studies of compressible flow in 3D for very fine meshes, to investigate possible blowup beyond the mesh resolutions currently available.

This paper is organized in the following way: in Section 2 we introduce the Navier-Stokes and the Euler equations, and in Section 3 we discuss vorticity and differences in 2D and 3D. In Section 4 we describe an adaptive finite element method including a posteriori error estimation with a dual problem. We use this adaptive method for numerical experiments presented in Section 5, where the stability of the dual problem for flow past a circular cylinder is studied for different Mach numbers. We conclude with a summary of our findings in Section 6.

2. The basic equations. Let Ω be a fixed (open) domain in \mathbb{R}^d , $d = 2, 3$, with boundary Γ and let $I = [0, \hat{t}]$ be a time interval with initial time 0 and final time \hat{t} , and set $Q = \Omega \times I$. We seek density ρ , momentum $\mathbf{m} = \rho\mathbf{u}$ and total energy E , with velocity $\mathbf{u} = \mathbf{u}_i = (\mathbf{u}_1, \dots, \mathbf{u}_d)$, for $(\mathbf{x}, t) \in Q$, with $\mathbf{x} = \mathbf{x}_i = (\mathbf{x}_1, \dots, \mathbf{x}_d)$. The compressible Navier-Stokes equation without source terms for a perfect gas with appropriate boundary conditions read: find $\hat{\mathbf{u}} = (\rho, \mathbf{m}, E)$ such that

$$\begin{aligned} \partial_t \hat{\mathbf{u}} + \nabla \cdot \mathbf{f}(\hat{\mathbf{u}}) - \nabla \cdot \mathbf{f}_{visc}(\hat{\mathbf{u}}) &= 0 & \text{in } Q, \\ \hat{\mathbf{u}}(\cdot, 0) &= \hat{\mathbf{u}}_0 & \text{in } \Omega, \end{aligned} \quad (2.1)$$

where $\partial_t \hat{\mathbf{u}} = \frac{\partial \hat{\mathbf{u}}}{\partial t}$, and the fluxes are defined as

$$\mathbf{f}(\hat{\mathbf{u}}) = \begin{pmatrix} \rho\mathbf{u} \\ \mathbf{m} \otimes \mathbf{u} + p\mathbb{I} \\ (E + p)\mathbf{u} \end{pmatrix}, \quad \mathbf{f}_{visc}(\hat{\mathbf{u}}) = \begin{pmatrix} 0 \\ 2\mu\varepsilon(\mathbf{u}) + \lambda(\nabla \cdot \mathbf{u})\mathbb{I} \\ (2\mu\varepsilon(\mathbf{u}) + \lambda(\nabla \cdot \mathbf{u})) \cdot \mathbf{u} + \kappa\nabla T \end{pmatrix}, \quad (2.2)$$

with $\hat{\mathbf{u}}_0 = \hat{\mathbf{u}}_0(\mathbf{x})$ given initial data, and where \mathbb{I} is the identity matrix in \mathbb{R}^d , \otimes denotes the tensor product. The pressure p is defined from the state equation of a perfect gas:

$$p = (\gamma - 1)\rho T, \quad T = \left(\frac{E}{\rho} - \frac{1}{2}|\mathbf{u}|^2 \right), \quad (2.3)$$

where $(\gamma - 1)$ is the adiabatic gas constant, T is a temperature and $|\mathbf{u}|^2 = \sum_i \mathbf{u}_i^2$,

$$\varepsilon(\mathbf{u}) = \frac{1}{2}(\nabla\mathbf{u} + \nabla\mathbf{u}^T)$$

is the strain rate tensor and $\kappa \geq 0$ the thermal conduction parameter. The viscosity parameters are assumed to satisfy the conditions $\mu > 0$, $\lambda + 2\mu > 0$. We define the speed of sound as

$$c = \sqrt{\frac{p\gamma}{\rho}}.$$

For high Reynolds numbers the flow can be modeled by the compressible Euler equations: find $\hat{\mathbf{u}} = (\rho, \mathbf{m}, E)$ such that

$$\begin{aligned} \partial_t \hat{\mathbf{u}} + \nabla \cdot \mathbf{f}(\hat{\mathbf{u}}) &= 0 & \text{in } Q, \\ \hat{\mathbf{u}}(\cdot, 0) &= \hat{\mathbf{u}}_0 & \text{in } \Omega. \end{aligned} \quad (2.4)$$

3. Vorticity. For the present discussion we focus on the Euler equations, for simplicity, as a model for high Re number flow, which we can write as:

$$\partial_t \rho + \nabla \cdot (\mathbf{u}\rho) = 0 \quad \text{in } Q, \quad (3.1)$$

$$\partial_t \mathbf{m} + \nabla \cdot (\mathbf{m} \otimes \mathbf{u}) + \nabla p = 0 \quad \text{in } Q, \quad (3.2)$$

$$\partial_t E + \nabla \cdot (\mathbf{u}E + \mathbf{u}p) = 0 \quad \text{in } Q. \quad (3.3)$$

Mass conservation (3.1) gives that we can write the momentum equation (3.2) as:

$$\partial_t \mathbf{u} + (\mathbf{u} \cdot \nabla) \mathbf{u} + \rho^{-1} \nabla p = 0. \quad (3.4)$$

Assuming that the solution to (3.4) is differentiable, we can derive an equation for the *vorticity* $\boldsymbol{\omega} = \nabla \times \mathbf{u}$, in the form of a linear convection-reaction system, which takes p , ρ and \mathbf{u} as coefficients:

$$\partial_t \boldsymbol{\omega} + (\mathbf{u} \cdot \nabla) \boldsymbol{\omega} - (\boldsymbol{\omega} \cdot \nabla) \mathbf{u} + \boldsymbol{\omega} (\nabla \cdot \mathbf{u}) = \frac{1}{\rho^2} \nabla \rho \times \nabla p. \quad (3.5)$$

Here the vortex stretching term $(\boldsymbol{\omega} \cdot \nabla) \mathbf{u}$ corresponds to the basic mechanism in turbulence that transfers energy from large to small scales, to eventually dissipate as heat at the smallest scales. We also note the baroclinic vector $\frac{1}{\rho^2} \nabla \rho \times \nabla p$, which acts as a source of vorticity in areas where the gradients of density and pressure are not aligned.

For incompressible flow with constant density, the baroclinic vector is zero and the vorticity equation reduces to:

$$\partial_t \boldsymbol{\omega} + (\mathbf{u} \cdot \nabla) \boldsymbol{\omega} - (\boldsymbol{\omega} \cdot \nabla) \mathbf{u} = 0. \quad (3.6)$$

Thus for incompressible flow, the only source of vorticity is the boundary conditions. No slip boundary conditions can generate vorticity in the resulting boundary layer, whereas slip boundary conditions create no vorticity. On the other hand, the vortex stretching term can lead to high local growth of vorticity from small perturbations, see [22].

In 2D, the vorticity equation takes the form:

$$\partial_t \boldsymbol{\omega} + (\mathbf{u} \cdot \nabla) \boldsymbol{\omega} + \boldsymbol{\omega} (\nabla \cdot \mathbf{u}) = \frac{1}{\rho^2} \nabla \rho \times \nabla p. \quad (3.7)$$

Vorticity in 2D is a scalar, and there is no vortex stretching term. In particular, no turbulent dissipation by vortex stretching is thus possible for high Re flow in 2D.

4. Adaptive finite element method. We now recall an adaptive finite element method for the time dependent compressible Euler/Navier-Stokes equations, developed in [28, 27, 29]. We highlight the role of the dual problem for a posteriori error estimation, and we present an adaptive algorithm which we use in our computational study.

4.1. Discretization of the primal problem. Let $0 = t_0 < t_1 < \dots < t_N = \hat{t}$, be a sequence of discrete time steps with associated time intervals $I_n = (t_{n-1}, t_n]$ of length $\Delta t_n = t_n - t_{n-1}$, and let $W_h \subset H^1(\Omega)$ be a finite element space consisting of continuous piecewise linear functions on a fixed mesh $\mathcal{T}_h = \{K\}$ of mesh size $h_K < 1$, with triangular elements K . We first discretize the equations in space by a finite

element method, and we then solve the resulting system in time with a 3rd order explicit Runge-Kutta method.

The finite element approximation of the compressible Euler equations (2.4) reads: find $\hat{\mathbf{u}}_h = \hat{\mathbf{u}}_h(t) \equiv (\rho_h(t), \mathbf{m}_h(t), E_h(t))$ with $\hat{\mathbf{u}}_h(t) \in \mathbf{X}_h \equiv W_h \times W_h^d \times W_h$, such that

$$(\partial_t \hat{\mathbf{u}}_h, \hat{\mathbf{v}}_h) + (\nabla \cdot \mathbf{f}(\hat{\mathbf{u}}_h), \hat{\mathbf{v}}_h) + (\mathbf{f}_{h,visc}(\hat{\mathbf{u}}_h), \nabla \hat{\mathbf{v}}_h) = 0, \quad (4.1)$$

for all test functions $\hat{\mathbf{v}}_h = (v_h^p, v_h^m, v_h^e) \in \mathbf{X}_h$, where

$$(\mathbf{v}, \mathbf{w}) = \sum_{K \in \mathcal{T}_h} \int_K \mathbf{v} \cdot \mathbf{w} \, dx.$$

The resulting system of ordinary differential equations (ODE) is solved by the Runge-Kutta method RK3. We denote by $\hat{\mathbf{u}}_n$ the solution at the discrete time steps t_n , that is $\hat{\mathbf{u}}_n \equiv \hat{\mathbf{u}}_h(t_n)$.

We define \mathbf{u}_n , p_n and T_n to be finite element functions in W_h^d , W_h and W_h , respectively, defined by their nodal values at time $t = t_n$:

$$\begin{aligned} \mathbf{u}_n(\mathbf{N}_i) &= \mathbf{m}_n(\mathbf{N}_i) / \rho_n(\mathbf{N}_i), \\ p_n(\mathbf{N}_i) &= (\gamma - 1) \rho_n(\mathbf{N}_i) T_n(\mathbf{N}_i), \\ T_n(\mathbf{N}_i) &= E_n(\mathbf{N}_i) / \rho_n(\mathbf{N}_i) - |\mathbf{u}_n(\mathbf{N}_i)|^2 / 2 \end{aligned} \quad (4.2)$$

for all nodes \mathbf{N}_i in the mesh \mathcal{T}_h .

The method is stabilized by adding entropy viscosity, described in [12], where the viscous fluxes at $t = t_n$ are approximated as:

$$\mathbf{f}_{h,visc}(\hat{\mathbf{u}}_h) = \begin{pmatrix} \nu_n \nabla \rho_n \\ \mu_n \varepsilon(\mathbf{u}_n) \\ \mu_n \varepsilon(\mathbf{u}_n) \cdot \mathbf{u}_n + \kappa_n \nabla T_n \end{pmatrix}. \quad (4.3)$$

The entropy functional is defined as

$$S_n(p_n, \rho_n) = \frac{\rho_n}{\gamma - 1} \log \left(\frac{p_n}{\rho_n^\gamma} \right).$$

Let Δt be a constant time-step and S_n, S_{n-1}, S_{n-2} be the value of the entropy functional at times t_n, t_{n-1}, t_{n-2} respectively. Then, at each time step the entropy residual is computed for each mesh cell K in \mathcal{T}_h and is then used for computation of the artificial viscosity:

$$\mathcal{R}(S_n) := \frac{1}{2\Delta t} (3S_n - 4S_{n-1} + S_{n-2}) + \nabla \cdot (\mathbf{u}_n S_n), \quad (4.4)$$

$$\mu_E|_K := c_E \|\rho_n\|_{\infty, K} h_K^2 \|\mathcal{R}(S_n)\|_{\infty, K}. \quad (4.5)$$

The maximum artificial viscosity, μ_{\max} , is determined as follows:

$$\mu_{\max}|_K = c_{\max} h_K \|\rho_n\|_{\infty, K} \|\mathbf{u}_n\| + c_n \|c_n\|_{\infty, K}, \quad (4.6)$$

with c_n the speed of sound. Finally we set:

$$\begin{aligned} \mu_n|_K &= \max [\min(\mu_{\max}|_K, \mu_E|_K), \mu_{phys}], \\ \kappa_n|_K &= \frac{\mathcal{P}}{\gamma - 1} \mu_n|_K, \quad \nu_n|_K = \frac{\mathcal{P}_\rho}{\|\rho_n\|_{\infty, K}} \mu_n|_K, \end{aligned} \quad (4.7)$$

where $\mathcal{P} \in [0, \frac{1}{4}]$ and $\mathcal{P}_\rho \in [0, \frac{1}{10}]$, $c_E = 1$ and $c_{\max} \in [0.1, 0.5]$ according to [11, 12]. And μ_{phys} is a physical viscosity coefficient which is zero for the inviscid computations.

4.2. Dual problem. We introduce the following dual problem, see [27]: Find $\Phi = (\phi_\rho, \phi_{\mathbf{m}}, \phi_E)$ such that

$$\begin{aligned} -\partial_t \Phi - \mathbf{f}'(\hat{\mathbf{u}}_h)^T \nabla \Phi &= \Psi_Q && \text{in } Q, \\ (\mathbf{n} \cdot \mathbf{f}'(\hat{\mathbf{u}}_h))^T \Phi &= \Psi_\Gamma && \text{on } \Gamma \times I, \\ \Phi(\cdot, \hat{t}) &= 0 && \text{in } \Omega, \end{aligned} \quad (4.8)$$

where ϕ_ρ is *dual density*, $\phi_{\mathbf{m}}$ *dual momentum* and ϕ_E *dual energy*, $\mathbf{f}'(\hat{\mathbf{u}}_h)^T$ is the transpose of the Jacobian matrix $\mathbf{f}'(\hat{\mathbf{u}}_h)$, and $\Psi \equiv \{\Psi_Q, \Psi_\Gamma\}$ are source terms with $\Psi_Q \in L_2(I; L_2(\Omega) \times [L_2(\Omega)]^d \times L_2(\Omega))$ and $\Psi_\Gamma \in L_2(I; L_2(\Gamma) \times [L_2(\Gamma)]^d \times L_2(\Gamma))$, which define a linear target functional by

$$\mathcal{M}(\hat{\mathbf{u}}) = \int_Q \hat{\mathbf{u}} \cdot \Psi_Q \, dx \, dt + \int_I \int_\Gamma \hat{\mathbf{u}} \cdot \Psi_\Gamma \, dS \, dt. \quad (4.9)$$

The expression $\mathbf{n} \cdot \mathbf{f}'(\hat{\mathbf{u}}_h)$ is referred to as the normal flux Jacobian. Boundary conditions for the dual problem are chosen based on the target functional and the boundary conditions of the primal equation.

4.3. The finite element discretization of the dual problem. Since we cannot solve the continuous problem (4.8) analytically, we replace Φ by a finite element approximation. Assuming homogeneous Dirichlet boundary conditions, for simplicity, we discretize the dual problem (4.8) in space by piecewise linear continuous finite elements, where we seek a function $\Phi_h = \Phi_h(t) = (\phi_{\rho_h}, \phi_{\mathbf{m}_h}, \phi_{E_h}) \in \mathbf{X}_h \equiv W_h \times W_h^d \times W_h$, such that

$$(-\partial_t \Phi_h - \mathbf{f}'(\hat{\mathbf{u}}_h)^T \nabla \Phi_h, \hat{\mathbf{v}}_h) + (\mathbf{f}_{visc}(\Phi_h), \nabla \hat{\mathbf{v}}_h) = (\Psi_Q, \hat{\mathbf{v}}_h), \quad (4.10)$$

for all test functions $\hat{\mathbf{v}}_h = (\mathbf{v}_h^{\phi_\rho}, \mathbf{v}_h^{\phi_{\mathbf{m}}}, \mathbf{v}_h^{\phi_E}) \in \mathbf{X}_h$. The ODE system (4.10) is solved by time stepping to get approximations $\Phi_n \equiv \Phi_h(t_n)$ for each discrete time t_n .

The dual equations are stabilized at $t = t_n$ by adding artificial viscous fluxes:

$$\mathbf{f}_{visc}(\Phi_h) = \begin{pmatrix} \nu_n \nabla \phi_{\rho_n} \\ \mu_n \nabla \phi_{\mathbf{m}_n} \\ \kappa_n \nabla \phi_{E_n} \end{pmatrix}, \quad (4.11)$$

with the stabilization parameters

$$\begin{aligned} \mu_{\max}|_K &= c_{\max} h_K \| |\mathbf{u}_n| + c_n \|_{\infty, K}, \\ \nu_n|_K &= \min(\mu_{\max}, c_E h_K^2 \| \mathcal{R}_{\phi_{\rho_n}}(\Phi_n) \|_{\infty, K} / \| \phi_{\rho_n} - \bar{\phi}_{\rho_n} \|_{\infty, \Omega}), \\ \mu_n|_K &= \min(\mu_{\max}, c_E h_K^2 \| \mathcal{R}_{\phi_{\mathbf{m}_n}}(\Phi_n) \|_{\infty, K} / \| \phi_{\mathbf{m}_n} - \bar{\phi}_{\mathbf{m}_n} \|_{\infty, \Omega}), \\ \kappa_n|_K &= \min(\mu_{\max}, c_E h_K^2 \| \mathcal{R}_{\phi_{E_n}}(\Phi_n) \|_{\infty, K} / \| \phi_{E_n} - \bar{\phi}_{E_n} \|_{\infty, \Omega}), \end{aligned} \quad (4.12)$$

where $\bar{g} = \frac{1}{|\Omega|} \int_\Omega g$ is the average of the corresponding quantity, and the residuals at time $t = t_n$ are defined as

$$(\mathcal{R}_{\phi_{\rho_n}}(\Phi_n), \mathcal{R}_{\phi_{\mathbf{m}_n}}(\Phi_n), \mathcal{R}_{\phi_{E_n}}(\Phi_n)) = -(\partial_t \Phi_n + \mathbf{f}'(\hat{\mathbf{u}}_n)^T \nabla \Phi_n - \Psi_Q). \quad (4.13)$$

The finite element discretization of the dual problem (4.10) involves the solution of the discretized primal equations $\hat{\mathbf{u}}_n$, reconstructed in time by linear interpolation. The transpose of the Jacobian in the above discretization (4.10) has the same characteristic values (speeds) as that of the primal compressible Euler equations. Therefore we use the same local wave speed as in (4.7) for the upper bound of the viscosity in the stabilization (4.12).

4.4. Time discretization. In the computational study we have tested different methods for time discretization of the dual problem (4.10): the first order implicit Euler method, the second order implicit Crank-Nicholson method, and explicit Runge-Kutta methods of orders 1, 2, 3 and 4. For all these tests we use either first order h -viscosity stabilization, or residual based viscosity defined in (4.12). We present results of different temporal discretization later in Section 5.4.1. Before linearization of the dual problem, we also performed tests where we averaged the primal solution $\hat{\mathbf{u}}_n$ by up to several levels of Clément interpolation [7, 1], to avoid blowup in the dual solution triggered by small numerical oscillations in the primal solution. Regardless of using different time-stepping techniques, stabilization and averaging, blowup in the dual solution is observed for the same Mach numbers in the numerical tests.

For the primal and dual problems, the time-step is calculated from the local cell diameter h and velocity \mathbf{u}_n : at time step t_n , the current time step is defined by

$$\Delta t_n = \text{CFL} \min_{K \in \mathcal{T}_h} \frac{h_K}{\|\mathbf{u}_h(t_n)\| + c_h(t_n)}_{\infty, K}, \quad (4.14)$$

for all elements K in the mesh \mathcal{T}_h . The CFL number in the numerical examples of this paper is typically chosen between 0.4 and 0.5.

4.5. Computation of drag coefficient. The drag coefficient for a body can be computed from:

$$C_{pd} = \frac{F_{pd}}{1/2 \rho_\infty |\mathbf{u}_\infty|^2 A}, \quad (4.15)$$

where $F_{pd} = \frac{1}{|I|} \int_I \int_{\Gamma_{body}} p(\mathbf{n} \cdot \mathbf{e}_{pd}) dS dt$ is the mean drag force over the time interval I , $\mathbf{e}_{pd} = (1, 0)^T$ is a unit vector in the flow direction, Γ_{body} is the surface of the body, ρ_∞ is the free stream density and \mathbf{u}_∞ is the free stream velocity of the fluid. A is a reference area, in this paper the diameter of the cylinder. We consider high Reynolds number compressible flows where pressure drag has the highest contribution to the total drag force, and thus we here neglect the shear stress contribution to drag. In this paper we use (4.15) to compute the drag coefficient of a 2D cylinder, although we note that alternatively a volume formulation may be used [18, 24, 9].

4.6. A posteriori error estimation and adaptive algorithm. The following a posteriori error estimate can be derived using standard techniques, see e.g. [15, 28, 16, 20]:

$$\begin{aligned} |\mathcal{M}(\hat{\mathbf{u}}) - \mathcal{M}(\hat{\mathbf{u}}_n)| &\leq \sum_n \sum_{K \in \mathcal{T}_n} \int_{I_n} C_h h_K |R(\hat{\mathbf{u}}_n)|_K \cdot |D\Phi|_K \\ &+ \sum_n \sum_{K \in \mathcal{T}_n} \int_{I_n} |Vis(\hat{\mathbf{u}}_n; \pi_h \Phi)_K| dt + h.o.t. \quad (4.16) \\ &\equiv \sum_{n, K} \mathcal{E}_n^K + h.o.t. \end{aligned}$$

where $\mathcal{M}(\hat{\mathbf{u}})$ is a target functional, $Vis(\hat{\mathbf{u}}_n; \mathbf{w}_h)_K$, for $\mathbf{w}_h \in X_h$, comes from the artificial viscosity stabilization, $\mathcal{R}(\hat{\mathbf{u}}_n) = \frac{1}{2\Delta t} (3\hat{\mathbf{u}}_n - 4\hat{\mathbf{u}}_{n-1} + \hat{\mathbf{u}}_{n-2}) + \nabla \cdot \mathbf{f}(\hat{\mathbf{u}}_n)$ is the residual of the Euler equations (2.4), $D\Phi$ is a space-time derivative of the dual solution Φ , $C_h = 1/2$ is an interpolation constant, and $h.o.t.$ denotes higher order

terms from the linearization. Furthermore, in practice the exact dual solution Φ is replaced with its finite element approximation Φ_h .

The drag force, which is computed from the surface integral of the body, is chosen as the target functional, so data for the dual problem is chosen as:

$$\begin{aligned}
\Psi_Q &= 0 && \text{in } Q, \\
\Psi_\Gamma \cdot (0, \mathbf{n}, 0) &= \frac{1}{|I|} (0, \mathbf{e}_{pd}, 0)^T && \text{on } \Gamma_{body} \times I, \\
\Psi_\Gamma \cdot (0, \mathbf{n}, 0) &= 0 && \text{on } \Gamma_{wall} \times I, \\
\Psi_\Gamma &= 0 && \text{on } \Gamma_{outflow} \times I, \\
\Phi(\cdot, \hat{t}) &= 0 && \text{in } \Omega.
\end{aligned} \tag{4.17}$$

Due to the choice of boundary conditions for the primal variables at inflow nothing is imposed for the dual variables. For detailed analysis of different target functional and boundary conditions for the adjoint problem, see [15].

An estimate of the error in the drag coefficient $\bar{\mathcal{E}}_{pd}$ is obtained by normalization of the error in the drag force:

$$\bar{\mathcal{E}}_{pd} = \frac{\sum_{n,K} \mathcal{E}_n^K}{1/2\rho_\infty |\mathbf{u}_\infty|^2 A}. \tag{4.18}$$

We can then formulate the following adaptive algorithm:

ALGORITHM 1. *Given a tolerance TOL, start from an initial coarse mesh \mathcal{T}_h^0 , with $k = 0$:*

- 1 *Compute an approximate primal solution on the mesh \mathcal{T}_h^k ;*
- 2 *Compute an approximate dual solution on the same mesh \mathcal{T}_h^k ;*
- 3 *Compute the error indicator defined in (4.16), if $\sum_{n,K} \mathcal{E}_n^K < TOL$, then STOP;*
- 4 *Refine a fixed fraction of cells in \mathcal{T}_h^k with largest error indicator to get a new mesh \mathcal{T}_h^{k+1} ;*
- 5 *Set $k = k + 1$ and go to 1.*

5. Computational study. In this section we present a computational study of the stability of the dual problem for flow past a circular cylinder in 2D. We perform the adaptive algorithm, with the source term in the dual problem corresponding to a posteriori estimation of the error in pressure drag defined above.

For each Mach number we solve the forward problem until $t = 6$. Since we are interested in fully developed solutions, we focus on the time interval $[3, 6]$, and thus starting from this final time we solve the dual problem backwards until $t = 3$.

At the end of each adaptive cycle 10% of the cells with the largest error contribution are refined. The stability factor $\mathcal{S} = \int_I \sum_K |D\Phi|_K dt$, and the estimate of the total error $\bar{\mathcal{E}}_{pd}$ are computed for every adaptive iteration. The total error $\bar{\mathcal{E}}_{pd}$ is estimated as the product of local errors in the form of residuals, and stability weights measuring local sensitivity through the solution to the dual problem, whereas the stability factor \mathcal{S} isolate the stability information, without multiplication with local errors. In Figure 5.1, the total error indicators $\bar{\mathcal{E}}_{pd}$ and the stability factors \mathcal{S} are computed for different Mach numbers as the mesh is refined, up to the finest mesh before blowup of the dual solution.

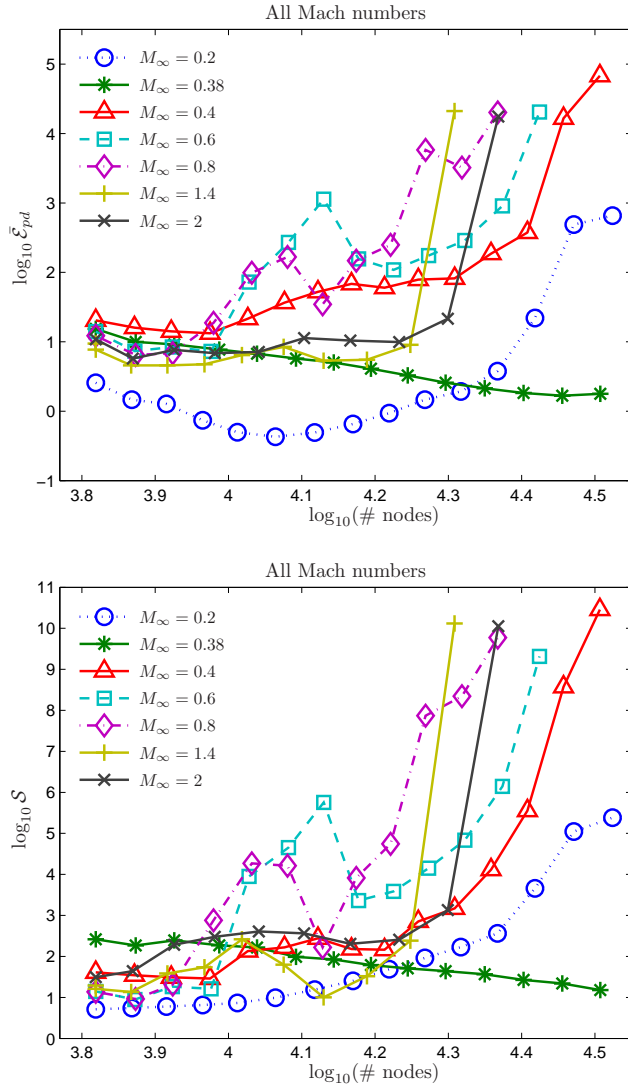


FIG. 5.1. \log_{10} of number of nodes versus \log_{10} of the total error $\bar{\mathcal{E}}_{pd}$, (above), and \log_{10} of number of nodes versus \log_{10} of the stability factor \mathcal{S} , (below), for different Mach numbers and boundary conditions.

5.1. Data and boundary conditions. The adaptive algorithm is performed for different Mach number regimes: subsonic flow $M_\infty = 0.2, 0.4$; transonic flow $M_\infty = 0.6, 0.8$; and supersonic flow $M_\infty = 1.4, 2.0$, and the following dimensionless variables are used: $\rho_\infty = \gamma = 1.4$, $p_\infty = 1$, $c_\infty = 1$, $\mathbf{u}_\infty = M_\infty$. We consider a 2D domain: a box of size 1.251×0.787 , with a circular cylinder of diameter 0.0254 located in the center of the box. The domain is uniformly triangulated by 6310 nodes and 12144 elements.

The following parameters are used in the time-stepping and the artificial viscosity: for the primal problem: $CFL = 0.4$, $c_E = 1$, $c_{\max} = 0.25$, $\mathcal{P}_\rho = 0.2$, $\mathcal{P} = 0.2$; for the

dual problem: $CFL = 0.4$, $c_E = 1$ or 2 , $c_{\max} = 0.1$ or 0.2 .

We have the following boundaries: inlet Γ_{inlet} , outlet Γ_{outlet} , wall Γ_{wall} , and cylinder surface Γ_{body} . We impose slip boundary conditions (reflecting boundary conditions) at the wall by requiring the normal component of the velocity to vanish, so that no mass or other convective fluxes can penetrate the wall:

$$\mathbf{u} \cdot \mathbf{n} = 0, \quad \text{on } \Gamma_{wall} \times I. \quad (5.1)$$

The outward normal \mathbf{n} is computed for each boundary node by taking a weighted average of the surrounding facet normals. We impose the slip boundary condition in strong form, that is, the boundary condition is applied after assembling the stiffness matrix and the load vector, where a row in the linear algebra system corresponding to a boundary node is replaced by a new row according to the boundary condition. Following Löhner [26] we apply characteristic based boundary conditions at inlet Γ_{inlet} and outlet Γ_{outlet} . Characteristic variables of the one-dimensional Euler equations are found locally in each boundary cell, which are then modified according to incoming waves to approximate non-reflecting boundary conditions.

For subsonic flow, no-slip boundary conditions are imposed on the cylinder surface, and we use a physical viscosity corresponding to a Reynolds number of $Re \approx 20\,000$ based on the cylinder diameter.

To reduce the geometry error in the approximation of the cylinder surface, we project the new nodes of the refinement to the exact boundary surface. See for instance Figure 5.2, which shows the initial mesh and the final mesh for the subsonic $M_\infty = 0.4$ simulation.

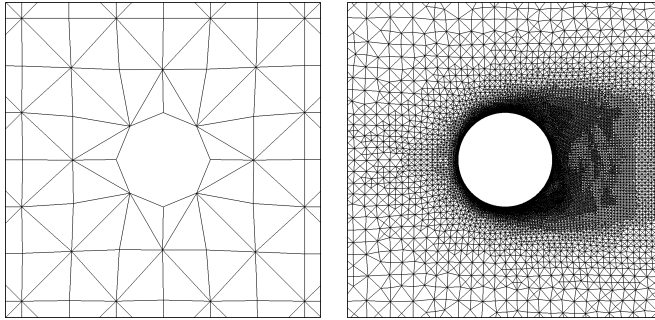


FIG. 5.2. $M_\infty = 0.4$; zoom of the initial mesh (left) and the mesh after 14th adaptive iterations (right), with 32 105 nodes and 63 088 cells.

5.2. Subsonic flow. For low Mach numbers we have subsonic flow, which we here model in two ways; either using the inviscid Euler equations with slip boundary conditions, or the viscid Navier-Stokes equations with no slip boundary conditions.

5.2.1. The inviscid case. We first consider subsonic flow around a cylinder at $M_\infty = 0.38$, where we use the inviscid Euler equations and slip boundary conditions. This problem has a stationary solution with zero drag coefficient, and is a standard test case for numerical methods, see e.g. [4]. The pressure and Mach number are symmetric across the cylinder.

Due to inaccuracy in the geometry representation of the cylinder boundary, numerical noise develops which generate unphysical vorticity. Bassi and Rebay [4] show that a highly accurate solution for DG methods can be obtained by using a high order

representation of the geometry. In this paper we use a linear approximation of the boundary, where we apply the slip boundary condition in strong form using a nodal based normal of the boundary. For coarse meshes we observe instabilities and spurious vorticity behind the cylinder, see Figure 5.3. The error in the geometry decreases when the mesh is adaptively refined. We obtain almost a symmetric shape for the Mach isolines for the finest mesh. The error estimate $\bar{\mathcal{E}}_{pd}$ is converging to zero, and the stability factor \mathcal{S} has a moderate size, see Figure 5.1. We observe no blowup in the dual solution as the mesh is refined.

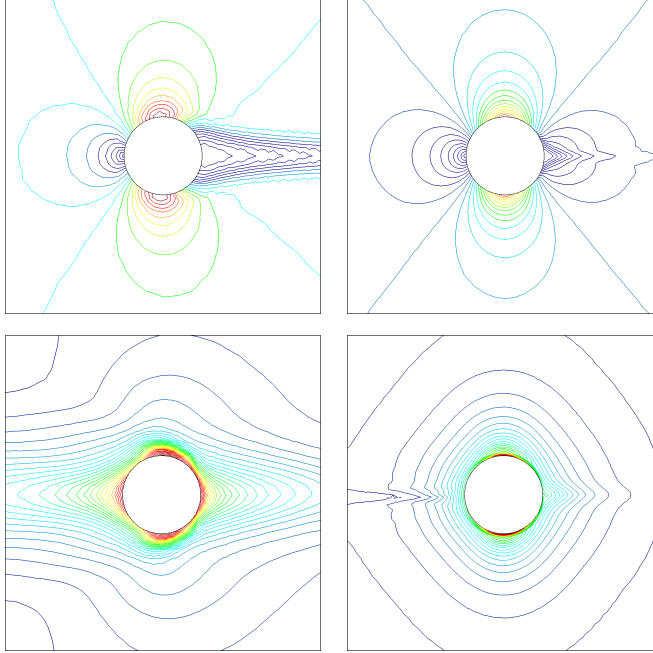


FIG. 5.3. *Inviscid subsonic flow*, $M_\infty = 0.38$. Isolines of Mach number starting from 0 and increasing with step 0.038 are from 5th adaptive iteration with 11 791 nodes and 23 239 cells, (top left), and 13th iteration, with 33 178 nodes and 65 622 cells, (top right), for $t = 6$. Isolines of magnitude of the corresponding dual momentum are plotted in the row below, with $|\phi_{\mathbf{m}}|_\infty = 1.14$ (left) and $|\phi_{\mathbf{m}}|_\infty = 2.23$ (right), for $t = 5$.

5.2.2. The viscous case. We consider subsonic flow at $M_\infty = 0.2$ and $M_\infty = 0.4$, where we use a physical viscosity corresponding to a Reynolds number of about 20 000 and no slip boundary conditions on the cylinder surface. For the initial iterations of the adaptive algorithm we observe that the estimate of the total error decreases, and the stability factors grow only moderately, see Figure 5.1. However, already after the 6th iteration the stability factors increase rapidly, resulting in divergence of the estimated error in drag. This is consistent with the computational results in [3], that indicate blowup of the dual problem for subsonic flow at increasing Reynolds numbers.

The vorticity and dual momentum are plotted in Figures 5.4 and 5.5. The top rows shows the solution of the 10th and 9th adaptive iterations respectively, and the lower row the solutions from one iteration before the blowup in the dual solution. In both cases we see that the growth in magnitude of the dual solution, is correlated with the sharpening of gradients and increase of vorticity in the primal solution as

the mesh is refined.

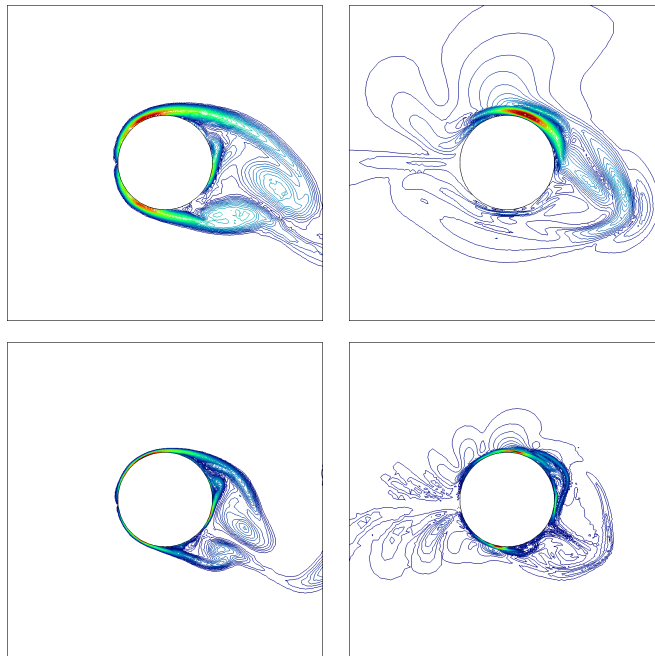


FIG. 5.4. *Viscous subsonic flow*, $M_\infty = 0.2$. *The first row: 10th iterations, 20 752 nodes and 41 032 cells, $|\omega|_\infty = 285.76$, $|\phi_m|_\infty = 26.74$; The second row: 14th iterations, 33 406 nodes and 65 895 cells, $|\omega|_\infty = 1\,185.343$, $|\phi_m|_\infty = 11\,764.07$.*

5.3. Transonic flow. For transonic flow with $M_\infty = 0.6$ and $M_\infty = 0.8$, we use the inviscid Euler equations with slip boundary conditions on the cylinder surface. The flow is characterized by trailing shock waves attached to the cylinder, where the main contribution to the drag force is the resulting pressure jump.

Due to the similarity of the solutions at these two Mach numbers, we here present plots only for $M_\infty = 0.8$. Figure 5.6 shows the vorticity and dual momentum for two adaptive iterations (the 6th and 11th iteration). The flow separates near the attached shock waves, where also the magnitude of vorticity is the highest, and the wake is rapidly oscillating. Similar to the viscous subsonic case, vorticity increases by mesh refinement, and the dual solution shows blowup which originates from the same region of the flow near separation of the primal solution.

5.4. Supersonic flow. Now we consider supersonic flow at the inlet with $M_\infty = 1.4$ and $M_\infty = 2$. The flow develops a detached bow shock upstream the cylinder, and attached trailing shock waves form behind the cylinder. The attached trailing shocks are more stable than for the transonic case, no rapid fluctuation is found. However, when the mesh is refined, we observe small fluctuations in the wake, and vorticity increases near the separation.

Figure 5.7 shows vorticity and dual momentum for the $M_\infty = 2$. For coarse meshes the dual solution shows no signs of blowup. The upper right plot of the figures indicate that the position of the bow shock has the highest impact for the accuracy of the drag force. The dual solution is convected upstream, and two waves travel toward the upper and lower wall boundaries and are then reflected.

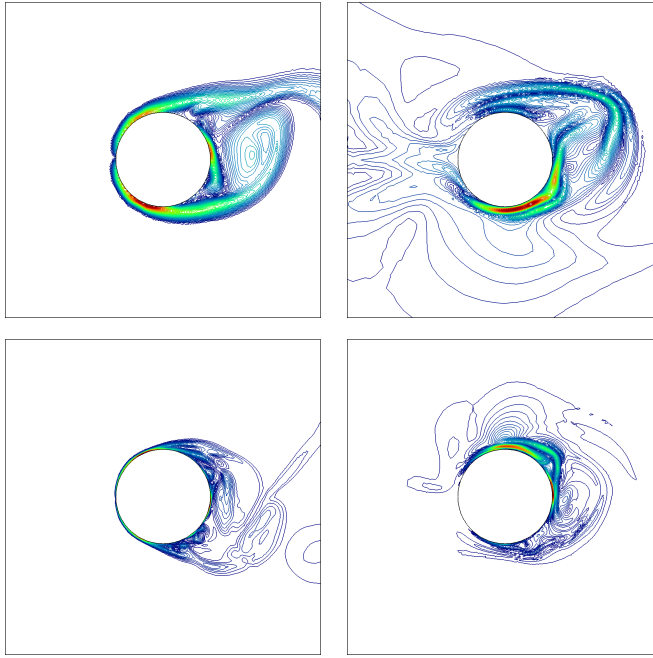


FIG. 5.5. *Viscous subsonic flow*, $M_\infty = 0.4$. The first row: 9th iterations, 18 156 nodes and 35 889 cells, $|\omega|_\infty = 499.78$, $|\phi_m|_\infty = 12.85$; The second row: 14th iterations, 32 105 nodes and 63 088 cells, $|\omega|_\infty = 2\,713.74$, $|\phi_m|_\infty = 531\,929.90$.

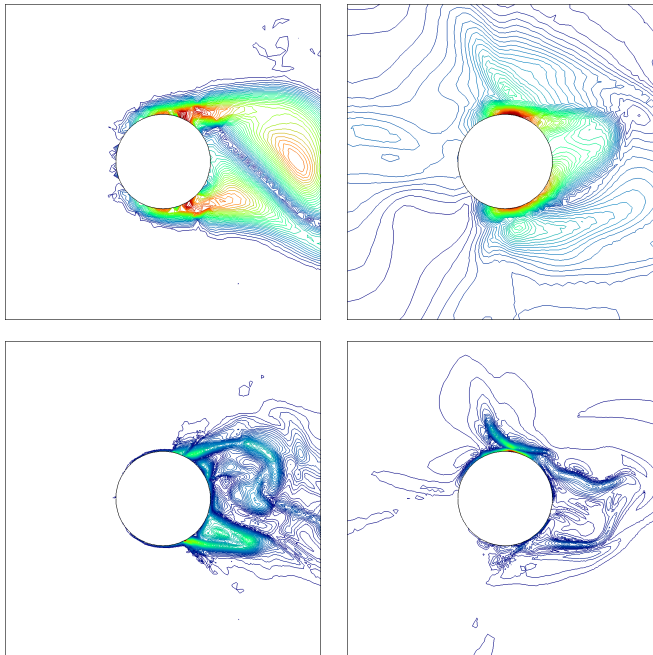


FIG. 5.6. *Inviscid transonic flow*, $M_\infty = 0.8$. The first row: 6th iterations, $t = 3$, 13 440 nodes and 26 552 cells, $|\omega|_\infty = 288$, $|\phi_m|_\infty = 12.44$; The second row: 11th iterations, $t = 2.1$, 23 305 nodes and 46 074 cells, $|\omega|_\infty = 834.56$, $|\phi_m|_\infty = 177\,355.87$.

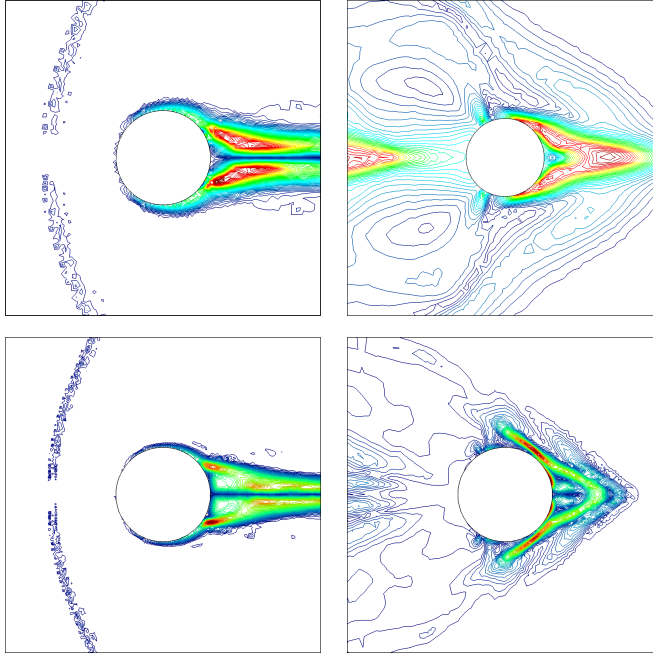


FIG. 5.7. *Inviscid supersonic flow*, $M_\infty = 2.0$. The first row: 7th iterations, $t = 3$, 17 098 nodes and 33 826 cells, $|\omega|_\infty = 486.67$, $|\phi_m|_\infty = 2.92$; The second row: 9th iterations, $t = 2.55$, 23 344 nodes and 46 242 cells, $|\omega|_\infty = 1\,044.18$, $|\phi_m|_\infty = 83\,569.0$.

But as the mesh is further refined, we again observe blowup in the dual solution originating near separation and the attached shocks.

5.4.1. Implicit time-stepping and uniform mesh refinement. The above computations are done using explicit 3rd order Runge-Kutta method for primal and dual problems. The artificial viscosity for both solvers are residual based. In this section we do the following tests: for a given Mach number $M_\infty = 1.4$ we solve the dual problem (a) with first order viscosity, (b) with an implicit scheme for time-stepping and (c) with uniform mesh refinement: after each cycle we refine the area inside a circle with radius 0.127 and located at the center of the cylinder uniformly.

Figure 5.8 is the result of the computation where the mesh is uniformly refined and Figure 5.9 is from the case where first order viscosity is used. Figure 5.10 shows the total estimated error and the stability factors as functions of the number of nodes for all different cases: EV means the explicit Runge-Kutta and high order viscosity; hV means the explicit Runge-Kutta and first order h -viscosity; Uniform means that the mesh is refined uniformly after each cycle where primal-dual problems are solved; Implicit means the implicit Crank-Nicholson method and h -viscosity is used in the dual computation. We observe that, regardless of using different time-stepping schemes, adaptive or uniform mesh refinements, linear or high order artificial viscosity, there is a blowup on the dual solution as the mesh resolution is fine enough.

6. Summary and conclusion. Stability of the dual problem is of key importance in goal oriented a posteriori error estimation, which is a basis for adaptive finite element methods. In this paper we have presented a computational study of the stability of the dual problem for 2D flow past a circular cylinder at various Mach

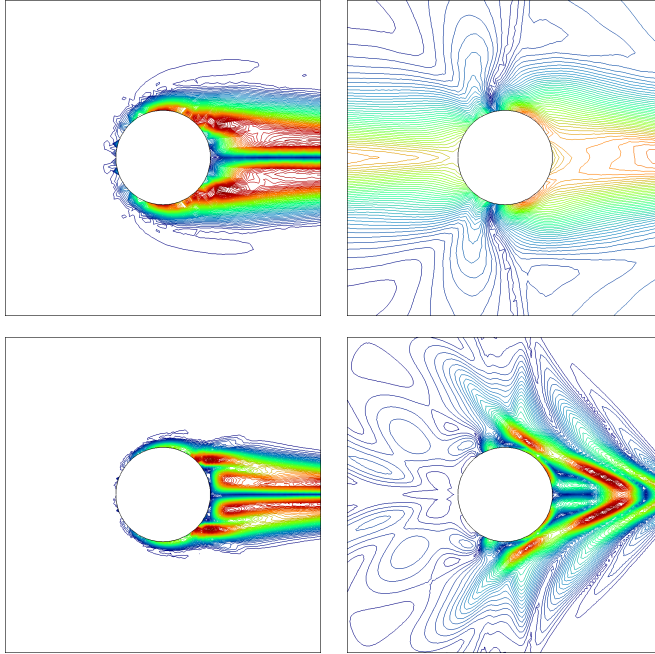


FIG. 5.8. *Inviscid supersonic flow*, $M_\infty = 1.4$, the mesh is refined uniformly after each iterations. The first row: 6th iterations, $t = 3$, 26 684 nodes and 53 084 cells, $|\omega|_\infty = 249.62$, $|\phi_m|_\infty = 1.737$; The second row: 8th iterations, $t = 2.85$, 86 753 nodes and 173 174 cells, $|\omega|_\infty = 501.13$, $|\phi_m|_\infty = 62\,161.19$.

numbers. Our results confirm previous reports of blowup of the dual problem, at certain Mach numbers for flow at high Reynolds numbers in 2D [3, 2].

In this paper we investigate the stability of the dual solution with respect to the computation of a mean drag force on the cylinder. For inviscid subsonic flow we have no blowup in the dual solution, and the adaptive algorithm converges towards the stationary solution. Although, for viscous subsonic flow at $Re \approx 20\,000$, we observe blowup as we refine the mesh, which is consistent with the findings in [2]. For transonic and supersonic flow, blowup is found when the mesh is refined beyond a certain resolution, where the source of instability is the region near separation at the attached shocks, which for transonic flow is oscillating rapidly. The position of the attached shock is of critical importance in the computation of drag, since the pressure drop over the shock is a significant part of the drag. For supersonic flow computed on coarse meshes, the position of the bow shock appears most important, whereas when the mesh is refined, the region near the attached shock dominates the dual problem.

We have tested various stabilization techniques and time stepping methods to solve the dual problem, which all show consistent results of blowup. Therefore, we are led to the conclusion that the blowup is not a result of an unstable discretization. Our hypothesis is instead that the continuous dual problem is unstable, likely connected to the primal solution at which the dual problem is linearized.

We also note that up until the dual solution blows up, it serves well as a basis for adaptive mesh refinement, where the mean drag force appears to converge, see Figure 5.11. We present the final meshes which are adaptively refined for the supersonic case in Figure 5.12.

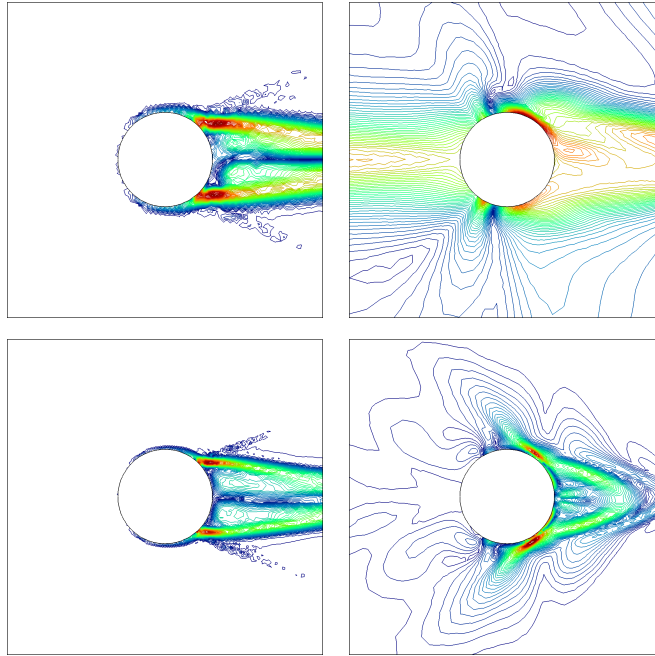


FIG. 5.9. *Inviscid supersonic flow*, $M_\infty = 1.4$, h -viscosity is used to stabilize the dual problem. The first row: 7th iterations, $t = 3$, 15 295 nodes and 30 275 cells, $|\omega|_\infty = 567.71$, $|\phi_m|_\infty = 1.76$; The second row: 9th iterations, $t = 2.625$, 20 130 nodes and 39 874 cells, $|\omega|_\infty = 1\,017.63$, $|\phi_m|_\infty = 104\,469.26$. h -viscosity is used to stabilize the dual problem.

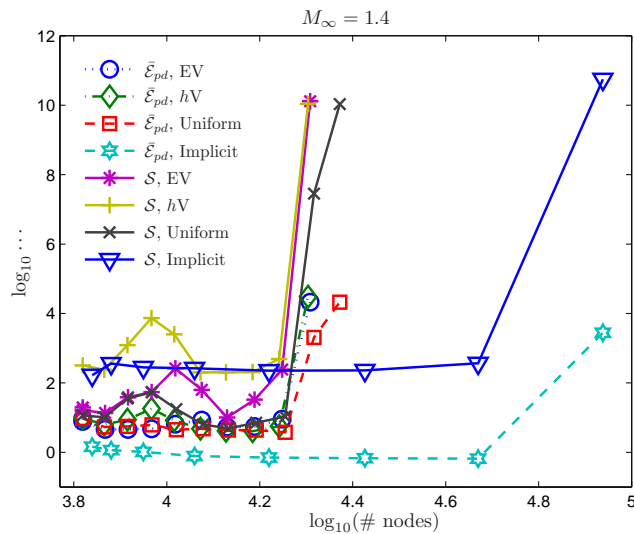


FIG. 5.10. \log_{10} of number of nodes versus \log_{10} of the total error $\bar{\mathcal{E}}_{pd}$ and \log_{10} of number of nodes versus \log_{10} of the stability factor S , for $M = 1.4$ with different ways of approximation of the dual problem and spatial mesh adaptations.

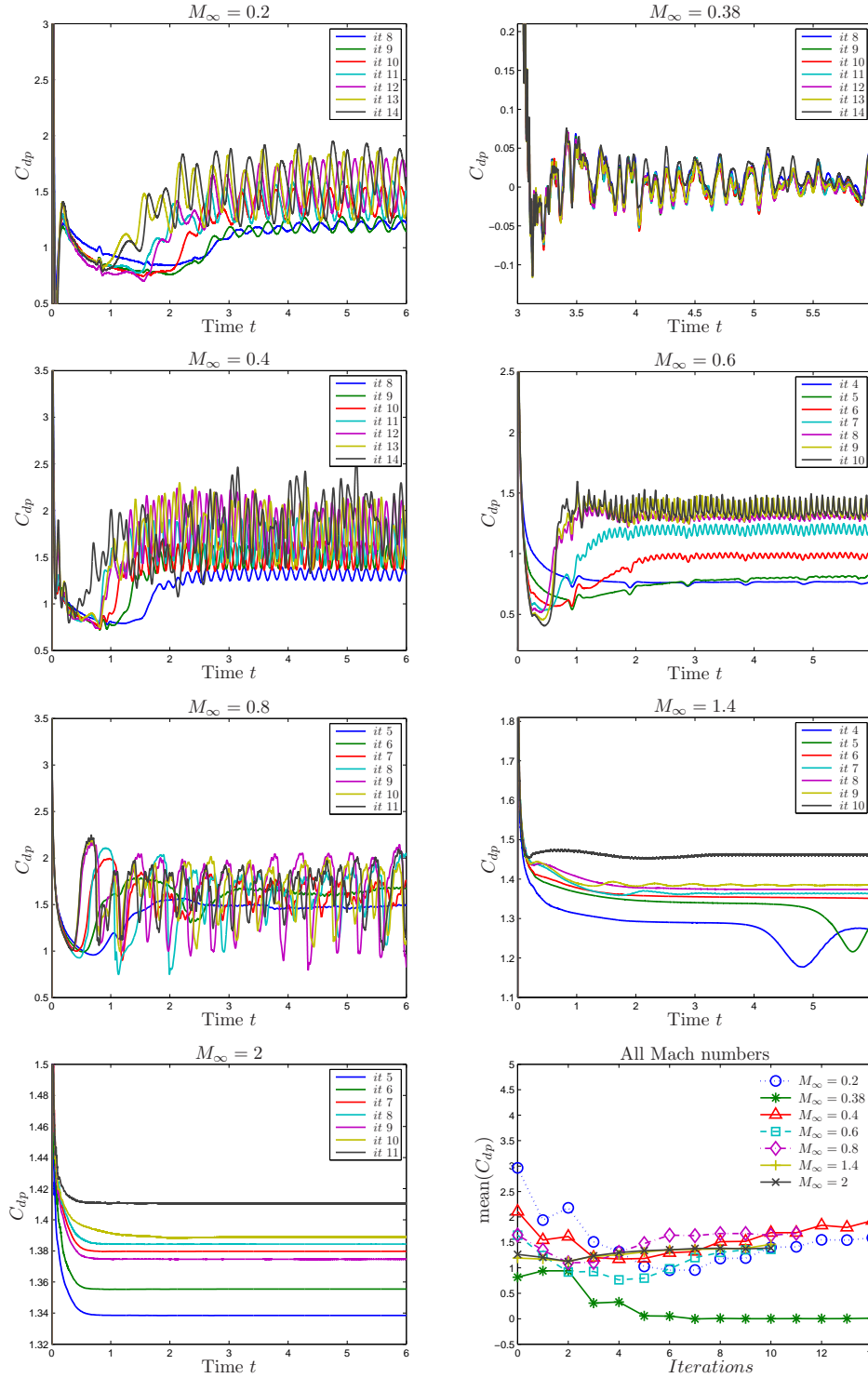


FIG. 5.11. Pressure drag coefficients C_{dp} on the finest adapted meshes from all computations. For subsonic viscous flow $M_\infty = 0.2, 0.4$ and transonic flow $M_\infty = 0.6, 0.8$, the curves oscillate more and obtain non-periodic motion as the mesh is refined. For supersonic flow, the curves are more stable: this could be due to stability of the attached shock waves on the boundary of the cylinder. The bottom-right figure shows the convergence of C_{dp} in the mean value for all Mach numbers.

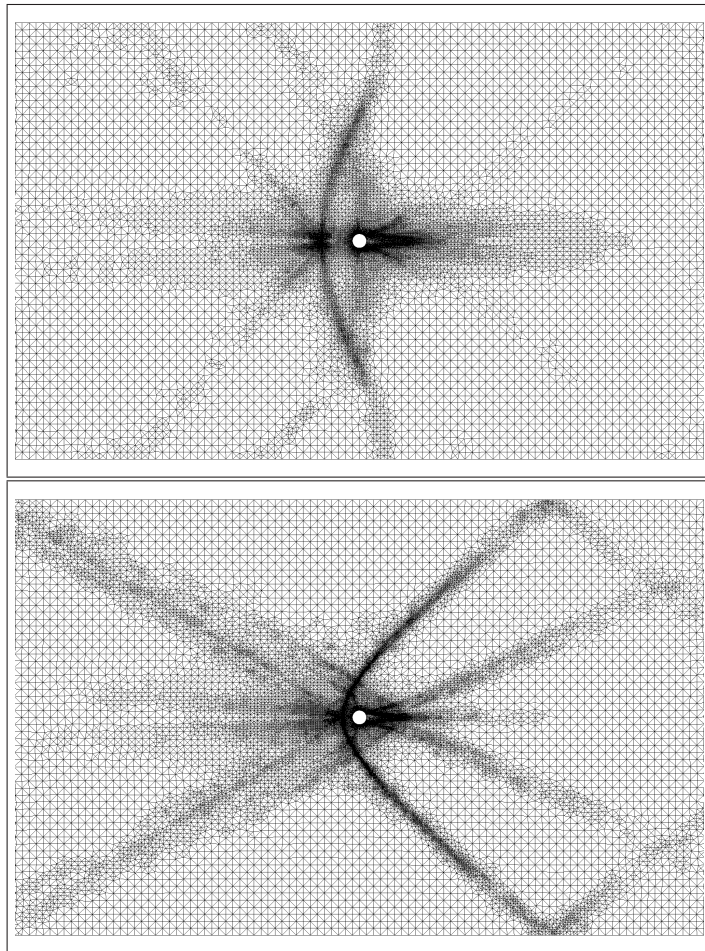


FIG. 5.12. *Supersonic flows: meshes after 9 adaptive iterations for $M_\infty = 1.4$ (above), and 11th iterations for $M_\infty = 2$ (below).*

For error estimation properties, the next question is then if blowup is the consequence of a linearization error from approximation of the exact primal solution, or if the underlying exact primal solution is unstable.

In work presented elsewhere we have solved dual problems in 3D, for compressible and incompressible flow, with no signs of blowup in the dual problem. In particular, we have computed incompressible turbulent flow in 3D using millions of mesh points [32, 23], for which the dual problem is stable. Similar studies in 3D for compressible flow will also be performed for very fine meshes, to investigate possible blowup beyond the mesh resolutions currently available.

We note that blowup in this paper is localized to regions near where the flow separates from the cylinder surface, and that these regions also show high vorticity production. In 2D no vortex stretching is possible, which is the basic mechanism for turbulent dissipation in 3D. For physical flow at high Reynolds numbers, 3D effects will develop, and thus a 2D model can be questioned. If the blowup in the dual solution is an indication of an unstable 2D flow, this condition could be useful to single out when a 2D model is unphysical.

We will follow up the present study, to get a better understanding of the stability of dual solutions in 2D and 3D, including the dependency on various flow parameters.

REFERENCES

- [1] ERN A AND GUERMOND J.-L., *Theory and Practice of Finite Elements*, Appl. Math. Sci. 159, Springer-Verlag, New York, 2004.
- [2] T. J. BARTH, *Space-Time Error Representation and Estimation in Navier-Stokes Calculations*, Lecture Notes in Computational Science and Engineering 56, 2007.
- [3] ———, *On the role of error and uncertainty in the numerical simulation of complex fluid flows*, 2010. SIAM Annual Meeting.
- [4] F. BASSI AND S. REBAY, *High-order accurate discontinuous finite element solution of the 2d euler equations*, J. Comput. Phys., 138 (1997), pp. 251–285.
- [5] R. BECKER AND R. RANNACHER, *A posteriori error estimation in finite element methods*, Acta Numer., 10 (2001), pp. 1–103.
- [6] E. BURMAN, *Adaptive finite element methods for compressible flow*, Computer methods in applied mechanics and engineering, 190 (2000), pp. 1137–1162.
- [7] P. CLÉMENT, *Approximation by finite element functions using local regularization*, RAIRO Anal. Numer., 9 (1975), pp. 77–84.
- [8] K. ERIKSSON, D. ESTEP, P. HANSBO, AND C. JOHNSON, *Introduction to adaptive methods for differential equations*, Acta Numer., 4 (1995), pp. 105–158.
- [9] M. GILES, M. LARSON, M. LEVENSTAM, AND E. SÜLI, *Adaptive error control for finite element approximations of the lift and drag coefficients in viscous flow*, Technical Report NA-76/06, Oxford University Computing Laboratory, (1997).
- [10] M. GILES AND E. SÜLI, *Adjoint methods for pdes: a posteriori error analysis and postprocessing by duality*, Acta Numer., 11 (2002), pp. 145–236.
- [11] J.-L. GUERMOND AND R. PASQUETTI, *Entropy-based nonlinear viscosity for fourier approximations of conservation laws*, C. R. Acad. Sci., Ser. I, 346 (2008), pp. 801–806.
- [12] J.-L. GUERMOND, R. PASQUETTI, AND B. POPOV, *Entropy viscosity method for nonlinear conservation laws*, J. Comput. Phys., 230(2011) (2011), pp. 4248–4267.
- [13] R. HARTMANN AND P. HOUSTON, *Adaptive discontinuous Galerkin finite element methods for nonlinear hyperbolic conservation laws*, SIAM J. Sci. Comp., 24 (2002), pp. 979–1004.
- [14] ———, *Adaptive discontinuous Galerkin finite element methods for the compressible Euler equations*, J. Comp. Phys., 183 (2002), pp. 508–532.
- [15] ———, *Error estimation and adaptive mesh refinement for aerodynamic flows*, in VKI LS 2010-01: 36th CFD/ADIGMA course on hp-adaptive and hp-multigrid methods, Oct. 26-30, 2009, H. Deconinck, ed., Von Karman Institute for Fluid Dynamics, Rhode Saint Genèse, Belgium, 2009.
- [16] J. HOFFMAN, *On duality based a posteriori error estimation in various norms and linear functionals for LES*, SIAM J. Sci. Comput., 26(1) (2004), pp. 178–195.
- [17] ———, *Computation of mean drag for bluff body problems using adaptive DNS/LES*, SIAM J. Sci. Comput., 27(1) (2005), pp. 184–207.
- [18] ———, *Adaptive simulation of the turbulent flow past a sphere*, J. Fluid Mech., 568 (2006), pp. 77–88.
- [19] ———, *Efficient computation of mean drag for the subcritical flow past a circular cylinder using General Galerkin G2*, International Journal of Numerical Methods in Fluids, 59(11) (2009), pp. 1241–1258.
- [20] J. HOFFMAN AND C. JOHNSON, *A new approach to computational turbulence modeling*, Comput. Meth. Appl. Engrg, 195 (2006), pp. 2865–2880.
- [21] ———, *Computational Turbulent Incompressible Flow*, Springer, 2007.
- [22] ———, *Resolution of d’alembert’s paradox*, J. Math. Fluid Mech., (Published Online First at www.springerlink.com: 10 December 2008).
- [23] N. JANSSON, J. HOFFMAN, AND M. NAZAROV, *Adaptive simulation of turbulent flow past a full car model*, in State of the Practice Reports, SC ’11, New York, NY, USA, 2011, ACM, pp. 20:1–20:8.
- [24] VOLKER JOHN, *Higher order finite element methods and multigrid solvers in a benchmark problem for the 3d navierstokes equations*, International Journal for Numerical Methods in Fluids, 40 (2002), pp. 775–798.
- [25] M.G. LARSON AND T J. BARTH, *A posteriori error estimation for discontinuous Galerkin approximations of hyperbolic systems*, In Discontinuous Galerkin Methods, B. Cockburn, G. Karniadakis, and C.-W. Shu, editors, Lecture Notes in Comput. Sci. Engrg., 11, Springer, Berlin, (2000), pp. 363–368.
- [26] R. LOHNER, *Applied CFD techniques: an introduction based on finite element methods*, John Wiley & Sons, 2001.
- [27] M. NAZAROV, J.-L. GUERMOND, AND B. PAPOV, *A posteriori error estimations for compressible*

- euler equations using entropy viscosity*, submitted, (2012).
- [28] M. NAZAROV AND J. HOFFMAN, *An adaptive finite element method for inviscid compressible flow*, International Journal for Numerical Methods in Fluids, 64 (2010), pp. 1102–1128.
 - [29] ———, *Residual-based artificial viscosity for simulation of turbulent compressible flow using adaptive finite element methods*, International Journal for Numerical Methods in Fluids, (2012).
 - [30] J. T. ODEN AND S. PRUDHOMME, *On goal-oriented error estimation for elliptic problems: Application to the control of pointwise errors*, Comput. Meth. Appl. Mech. Eng., 111 (1999), pp. 185–202.
 - [31] M. PARASCHIVOIU, J. PERAIRE, AND A. T. PATERA, *A posteriori finite element bounds for linear-functional outputs of elliptic partial differential equations*, Comput. Meth. Appl. Mech. Eng., 150 (1997), pp. 289–312.
 - [32] R. VILELA DE ABREU, N. JANSSON, AND J. HOFFMAN, *Adaptive computation of aeroacoustic sources for rudimentary landing gear*, in proceedings for Workshop on Benchmark problems for Airframe Noise Computations I, Stockholm, 2010.
 - [33] M.M. ZDRAVKOVICH, *Flow Around Circular Cylinders. Fundamentals, vol. 1.*, Oxford University Press, 1997.